RSC Advances

ROYAL SOCIETY OF CHEMISTRY

www.rsc.org/advances

A new approach to construct bulk and size-dependent continuous binary solution phase diagrams of alloys

N. Zhao[a], Y. Q. He*[b] and C. C. Yang*[a]

Abstract

The construct of bulk and size-dependent temperature-composition phase diagrams of alloys is critical for their industrial applications. However, the nano-phase diagrams are difficult to be determined accurately by experiments since the nano-phase equilibrium is metastable. In this work, a new approach was developed to construct both bulk and size-dependent continuous binary solution phase diagrams with three steps: (1) determining bulk atomic interaction energy by using *ab initio* molecular dynamics simulation; (2) calculating size-dependent melting enthalpy, melting temperature, and atomic interaction energy using a unified nanothermodynamics model; and (3) constructing phase diagrams with the above parameters, where a typical Au-Ag alloy was studied here as an example. It is found that (i) the simulated bulk atomic interaction energy is consistent with experimental data; (ii) the melting enthalpy, melting temperature, and atomic interaction energy decrease with decreasing material size for isolated nanocrystals; and (iii) the temperatures of solidus and liquidus curves drop and the two-phase zone becomes small for Au-Ag nanoalloy. The

[a]*Key Laboratory of Automobile Materials (Jilin University), Ministry of Education, and School of Materials Science and Engineering, Jilin University, Changchun 130022, China*

[b]*Cardiovascular Medicine, Sino-Japan Friendship Hospital, Jilin University, Changchun 130033, China*

**Corresponding authors. E-mails: hyq2@sina.com (Y. Q. He); ccyang@jlu.edu.cn (C. C. Yang).*

general approach developed here can be used to investigate other continuous binary alloy systems and can be extended to construct other phase diagrams, for example, the eutectic phase diagram.

1. Introduction

Until recently nanoalloys have been receiving great attentions due to their scientific and industrial importance even though single-component metallic nanocrystals have been extensively investigated. A number of reports have demonstrated that nanoalloys show superior physicochemical properties comparable to or even better than their alloy components.[1-4] For example, a recent study indicated that Au-Ag alloy nanoparticles (NPs) have a higher catalytic activity than pure Au and Ag NPs for CO oxidation.[1] Moreover, alloying is also an efficient approach to enhance the thermal stability of nanoscale materials.[3] As a result, the construct of bulk and size-dependent phase diagrams of alloys is of fundamental importance for their fabrications and industrial applications.[5-7] However, how to accurately determine the phase diagrams in experiments is a difficult task, especially at the nanometer scale, due to metastable nature of the nano-phase equilibrium.[8] As a result, theoretical modeling has become an attractive alternative approach in recent years. For example, several theoretical studies have been implemented to establish solid solution phase diagrams of nanosized binary alloys, which have larger surface/volume ratio than that of bulk alloys.[5,6,9-12] Wautelet et al.[5] developed a model to construct phase diagrams of Ge-Si nanoparticles by considering the size-dependent melting temperature $T_m(r)$ of pure elements, where r is the radius of nanoparticles and nanowires or half-thickness of thin films. It is found that both solidus and liquidus curves shift to lower temperatures compared to the bulk phase diagram. But, the size dependence of the melting enthalpy $H_m(r)$ was neglected in this model. Tanaka et al.[6] calculated binary

phase diagrams of nanoparticles by considering the composition- and temperature-dependent excess Gibbs energies and surface tensions of the solid and liquid phases with some rough approximations. Liang et al.[10] derived a model to establish phase diagrams of solid solution binary systems of metals Cu-Ni, semiconductors Ge-Si, ceramics Al_2O_3-Cr_2O_3 and V_2O_3-Cr_2O_3, and organic crystals *p*-chlorobromobenzene-*p*-dibromobenzene by considering $T_m(r)$, $H_m(r)$ and size-dependent atomic interaction energy $\Omega(r)$. It is found that the two-phase field shrinks with decreasing *r*. More recently, Guisbiers et al. presented phase diagrams of Au-Cu[11] and Cu-Ni[12] nanoparticles with considerations of effects of size, shape and surface segregation. Moreover, both experimental and theoretical efforts[13-17] have also been implemented to understand the size-dependent eutectic phase diagrams, which are more complicated than those of the solid solution. These approaches have contributed greatly to the basic understanding of nano-phase equilibria of different alloy systems. However, to date related reports on this topic are still limited and many challenges remain even for solid solution phase diagrams. For example, the critical parameters of bulk atomic interaction energy $\Omega^S(\infty)$ and $\Omega^L(\infty)$ are not considered or obtained from the known bulk phase diagrams in the above theoretical methods,[5,6,9-12] where ∞ denotes the bulk, and the superscripts L and S denote the liquid and solid, respectively. This has limited applications of these approaches.

In this work, a new approach was developed to construct both bulk and size-dependent continuous binary solution phase diagrams by combining *ab initio* molecular dynamics (MD) simulation and nanothermodynamics modeling. A typical

Au-Ag alloy system was studied here as an example due to its widespread applications in antibacterial materials,[18] catalysts,[19] sensors,[20] surface-enhanced Raman scattering,[21,22] etc.

2. Methodology

When a binary system is in a liquid-solid equilibrium state, the chemical potentials of component A (and B) in the both phases (solid and liquid phases) are equal. As a result, the solidus and liquidus curves of Au-Ag alloy system can be expressed by:[10]

$$H_{mB}(T_{mB}-T)/T_{mB} = \Omega^{S}(1-x_B^{S})^2-\Omega^{L}(1-x_B^{L})^2+RT\ln(x_B^{S}/x_B^{L}) \quad (1a)$$

$$H_{mA}(T_{mA}-T)/T_{mA} = \Omega^{S}(x_B^{S})^2-\Omega^{L}(x_B^{L})^2+RT\ln[(1-x_B^{S})/(1-x_B^{L})] \quad (1b)$$

where x is the mole fraction, T absolute temperature and R ideal gas constant. Eq. (1) can be utilized to (i) determine both x_B^{L} and x_B^{S} (or x_A^{L} and x_A^{S} with $x_A + x_B =1$) in a bulk phase diagram at a certain T when T_m, H_m, Ω^{S} and Ω^{L} are known; and (ii) calculate Ω^{S} and Ω^{L} when T, T_m, H_m, x_B^{L} and x_B^{S} are available from the bulk phase diagram. For the latter, Ω^{S} and Ω^{L} are generally determined at $T \approx (T_{mA}+T_{mB})/2$ as a first-order approximation since the composition effects on Ω^{S} and Ω^{L} are weak for continuous solution alloys due to small electronegativity difference between their components.[10] In this case, it is evident that a well-constructed bulk phase diagram measured in experiments is necessary if one wants to establish a size-dependent phase diagram. This has impeded the development of nanothermodynamics database. In this work, $\Omega^{S}(\infty)$ and $\Omega^{L}(\infty)$ will be obtained by *ab initio* MD simulations.

2.1 *Ab Initio* MD Simulations

Ω^S and Ω^L of regular solution are given by:[10]

$$\Omega^S = Z^S N_a \left(\varepsilon^S_{Au-Ag} - \frac{\varepsilon^S_{Au} + \varepsilon^S_{Ag}}{2} \right) \quad (2a)$$

$$\Omega^L = Z^L N_a \left(\varepsilon^L_{Au-Ag} - \frac{\varepsilon^L_{Au} + \varepsilon^L_{Ag}}{2} \right) \quad (2b)$$

where Z is the coordination number, N_a the Avogadro constant, and ε the bond strength.[10] ε can be determined by:

$$\varepsilon = \frac{2(E_t - NE_a)}{NZ} \quad (3a)$$

$$\varepsilon = \frac{2[E_t - AE_{aAu} - (N-A)E_{aAg}]}{NZ} \quad (3b)$$

where Eqs. (3a) and (3b) are for elemental crystals (Au and Ag) and alloys ($Au_{50}Ag_{50}$), respectively. Here, E_t is the total energy, E_a the single-atom energy, N the total number of atoms, A the number of Au atoms in $Au_{50}Ag_{50}$ solid solution. Note that Eq. (3) is applicable for pure metals or alloys in both solid and liquid states.

For geometry optimization, first-principles density functional theory (DFT)[23,24] calculations on Au, Ag and $Au_{50}Ag_{50}$ solid solution are implemented by using CASTEP code.[25] The exchange-correlation interaction was treated within the generalized gradient approximation (GGA) with Perdew-Burke-Ernzerhof (PBE) function.[26] All 4 atoms in the unit cells are fully relaxed with a convergence tolerance of 5×10^{-6} eV/atom of energy, 0.01 eV/Å of maximum force, and 5×10^{-4} Å of maximum displacement. The 8×8×8 k-points[27] were used to sample the Brillouin zone and the energy cutoff of 360 eV. The ultrasoft pseudopotential[28] was used for all

structures in the simulations. Based on the optimized systems, 3×3×3 supercells (Au, Ag and $Au_{50}Ag_{50}$ solid solution) with 108 atoms were built.

Then, the MD simulations were performed by using *ab initio* calculations. At first, the MD simulations were performed with NPT (dynamics with a thermostat to maintain a constant temperature and with a barostat to maintain a constant pressure). To characterize the liquid states, the constant temperatures are set as the melting points of Au, Ag and $Au_{50}Ag_{50}$, which are 1337, 1235 and 1306 K, respectively.[29] The simulated lattice parameters for liquid Au, Ag and $Au_{50}Ag_{50}$ are 4.397, 4.466 and 4.436 Å, respectively. The corresponding volume changes for the melting of Au, Ag and $Au_{50}Ag_{50}$ are 25.351%, 30.575% and 28.906%, respectively, which are much larger than the reported data of 1.2~6.8% for face-centered-cubic (FCC) structures.[30] Hence, these supercell structures cannot describe the liquid states accurately and the NPT method is invalid in this case. Alternatively, in this work, we conducted all MD simulations with NVT (dynamics at a fixed volume with a thermostat where a constant temperature is kept). The details will be given below.

The MD simulations with the NVT method were performed with the total simulation time and time step are 10.0 ps and 1.0 fs, respectively. The 2×2×2 k-points[27] were used to sample the Brillouin zone and the energy cutoff of 300 eV. The MD simulations were performed at T = 300 K, where the lattice parameters of a^S and a^L for the solid and liquid states, respectively, used in the simulations are listed in Table 1. For the solid states, the simulated results of E_t^S and E_a^S, and the calculation results of ε^S and Ω^S are also listed in Table 1. The corresponding solid structures of

Au, Ag and $Au_{50}Ag_{50}$ solid solution after MD simulations are plotted in Fig. 1. For the liquid states, Fig. 2 shows the supercell structures of liquid Au, Ag and $Au_{50}Ag_{50}$ after simulations. The simulated E_t^L and E_a^L, and the calculated ε^L and Ω^L are also given in Table 1.

2.2 Nanothermodynamics Modeling

In order to obtain the size-dependent phase diagrams of Au-Ag alloys, the size effects on these parameters in Eq. (1), T_m, H_m and Ω, should be considered. Recently, it has been revealed that vacancy formation determined by the cohesive energy variation is one of the intrinsic factors that dominate the variation of the potential profile and thus size-dependent physicochemical properties of low-dimensional nanocrystals.[8,34] Therefore, the size-dependent cohesive energy function $E_c(r)$ dominates the size dependence of a number of physicochemical properties of nanocrystals, including $T_m(r)$, $H_m(r)$ and $\Omega(r)$.

Combining the $E_c(r)$ function reported in the literature,[8,34] a universal relation can be obtained for isolated nanoparticles,

$$\frac{T_m(r)}{T_m(\infty)} = \frac{H_m(r)}{H_m(\infty)} = \frac{\Omega(r)}{\Omega(\infty)} = \frac{E_c(r)}{E_c(\infty)} = \left(1 - \frac{1}{4r/h - 1}\right)\exp\left(-\frac{2S_b}{3R}\frac{1}{4r/h - 1}\right) \quad (4)$$

where $S_b = E_b/T_b$ is bulk solid-vapor transition entropy of a crystal as determined by bulk solid-vapor transition enthalpy E_b and solid-vapor transition temperature T_b, and h the nearest atomic distance. Substituting Eq. (4) into Eq. (1), we can construct size-dependent Au-Ag phase diagrams.

3. Results and Discussions

As shown in Table 1, the simulation result of $\Omega^S(\infty)$ = -15828.562 J·mol^{-1} agrees well with the result [$\Omega^S(\infty)$ = -16402 J·mol^{-1}] obtained from experimental bulk Au-Ag phase diagram[35] with the deviation of only 3.5%. For $\Omega^L(\infty)$, the corresponding values are -14171.621 and -15599 J·mol^{-1},[35] respectively, and the deviation is 9.15%. Such a deviation may arise from (i) the assumption of composition independence of Ω (only $Au_{50}Ag_{50}$ was taken into account in this work); and (ii) the density value of liquid $Au_{50}Ag_{50}$ (average value of those of Au and Ag) used in the simulations. Nonetheless, the *ab initio* MD simulation results of $\Omega^S(\infty)$ and $\Omega^L(\infty)$ for Au-Ag alloys exhibit relative accuracy within 10% error. These data can thus be used to establish bulk Au-Ag phase diagram later.

Fig. 3 plots (1) bulk Au-Ag phase diagrams obtained in experiments;[35] (2) the calculation results of bulk and nanosized (r = 5 nm) Au-Ag phase diagrams from Eq. (1), where $T_m(r)$, $H_m(r)$ and $\Omega(r)$ are calculated from Eq. (4); and (3) experimental data of $T_m(r)$ of Au nanoparticles (r = 5 nm)[36] denoted as the symbols ∇ [$T_m(r)$ = 1169.4±63.5 and 1180.4±88.2 K] and a MD simulation result of $T_m(r)$ of Ag nanoparticles (r = 5 nm)[37] denoted as the symbol Δ [$T_m(r)$ = 1112.1 K]. As shown in the figure, the calculated bulk Au-Ag phase diagram from Eq. (1), where the simulation results of $\Omega^S(\infty)$ and $\Omega^L(\infty)$ are used in the modeling, is consistent with that measured in experiments within 3% error. Thus, our method provides a simple and effective way to calculate the interaction energy of continuous binary alloys.

It is clear that $T_m(r)$, $H_m(r)$ and $\Omega(r)$ all decrease with decreasing r according to

Eq. (4), indicating the instability of isolated nanoparticles compared with their counterparts in bulk materials. From Fig. 3, we can see that the model predictions of $T_m(r)$ are consistent with the experimental data of Au nanoparticles (r = 5 nm). Moreover, the derivation is only 5% between our calculation and the MD simulation results of $T_m(r)$ for Ag nanoparticles (r = 5 nm). These demonstrate the accuracy of Eq. (4). As r reducing, the surface/volume ratio increases, resulting in the formation of a large number of surface dangling bonds. Thus, the surface atoms are in a higher energetic state than those of the interior atoms, depressing $E_c(r)$, $T_m(r)$, $H_m(r)$ and $\Omega(r)$.

As shown in Fig. 3, the decreased $T_m(r)$ results in the drop of the solidus and liquidus curves, and the reduced $\Omega(r)$ causes the shrinkage of the two-phase zone in nanosized Au-Ag phase diagram compared with that of the bulk. The constructed size-dependent phase diagrams and these findings would be validated in future experimental studies. Our calculation results are critical for the basic understanding of the phase transition theory of nanoalloys and also for their scale-up industrial applications. If the necessary parameters are available, the general approach developed in this work could be used to establish other continuous binary alloy systems, and also be extended to construct other types of phase diagrams, for instance, the eutectic phase diagram. Moreover, it should be noted that only the size effect was focused in this work for a simplification. The dimensionality and shape effects could also be considered in our nanothermodynamics models,[8,34] which will be explored in future studies.

4. Conclusions

In summary, a simple and effective approach was developed to establish both bulk and size-dependent Au-Ag phase diagrams based on (1) bulk interaction energy $\Omega(\infty)$ calculated by *ab initio* MD simulations; and (2) size-dependent melting temperature $T_m(r)$, melting enthalpy $H_m(r)$, and interaction energy $\Omega(r)$ using a unified nanothermodynamics model. It is found that the simulated $\Omega(\infty)$ values are consistent with the results obtained from experimental bulk Au-Ag phase diagram. $T_m(r)$, $H_m(r)$ and $\Omega(r)$ all decrease with decreasing r for isolated Au and Ag nanoparticles, resulting in the drop of solidus and liquidus curves and shrinkage of the two-phase zone in nanosized Au-Ag phase diagram. The developed general approach could also be used to construct different phase diagrams in other alloy systems if the relevant parameters are available.

Acknowledgments

We wish to thank ChangBai Mountain Scholars Program and Jilin University Basic Research Grants Program for financially supporting this project and the computing resources of High Performance Computing Center of Jilin University and National Supercomputing Center in Jinan, China. We also thank G. Guisbiers for helpful discussions.

References

1 C. W. Yen, M. L. Lin, A. Q. Wang, S. A. Chen, J. M. Chen and C. Y. Mou, *J. Phys. Chem. C*, 2009, **113**, 17831-17839.

2 M. Oezaslan, M. Heggen and P. Sreasser, *J. Am. Chem. Soc*, 2012, **134**, 514-524.

3 T. Chookajorn, H. A. Murdoch and C. A. Schuh, *Science*, 2012, **337**, 951-954.

4 C. H. Cui, L. Gan, M. Heggen, S. Rudi and P. Strasser, *Nat. Mater.*, 2013, **12**, 765-771.

5 M. Wautelet, J. P. Dauchot and M. Hecq, *Nanotechnology*, 2000, **11**, 6-9.

6 T. Tanaka and S. Hara, *Metallkd*., 2001, **92**, 1236-1241.

7 A. van de Walle, Q. Hong, S. Kadkhodaei and R. Sun, *Nat. Commun.*, 2015, **6**, 7559.

8 Q. Jiang and Z. Wen, Thermodynamics of Materials, Higher Education Press, Beijing and Springer-Verlag Berlin Heidelberg, 2011.

9 R. Vallee, M. Wautelet, J. P. Dauchot and M. Hecq, *Nanotechnology*, 2001, **12**, 68-74.

10 L. H. Liang, D. Liu and Q. Jiang, *Nanotechnology*, 2003, **14**, 438-442.

11 G. Guisbiers, S. M. Rosales, S. Khanal, F. R. Zepeda, R. L. Whetten and M. J. Yacaman, *Nano Lett.*, 2014, **14**, 6718-6726.

12 G. Guisbiers, S. Khanal, F. R. Zepeda, J. R. de la Puente and M. J. Yacaman, *Nanoscale*, 2014, **6**, 14630-14635.

13 W. A. Jesser, R. A. Shneck and W. W. Gile, *Phys. Rev. B*, 2004, **69**, 144121.

14 J. G. Lee and H. Mori, *Phys. Rev. Lett.*, 2004, **93**, 235501.

15 J. Weissmuller, P. Bunzel and G. Wilde, *Scripta Mater.*, 2004, **51**, 813-818.

16 T. Ivas, A. N. Grundy, E. P. Karadeniz and L. J. Gauckler, *CALPHAD*, 2012, **36**, 57-64.

17 H. M. Lu and X. K. Meng, *Scientific Rep.*, 2015, **5**, 11263.

18 M. Banerjee, S. Sharma, A. Chattopadhyay and S. S. Ghosh, *Nanoscale*, 2011, **3**, 5120-5125.

19 H. L. Jiang, T. Akita, T. Ishida, M. Haruta and Q. Xu, *J. Am. Chem. Soc.*, 2011, **133**, 1304-1306.

20 J. I. Francisco and P. Z. Francis, *ACS Nano*, 2008, **2**, 1543-1552.

21 M. K. Fan, F. J. Lai, H. L. Chou, W. T. Lu, B. J. Hwang and A. G. Brolo, *Chem. Sci*., 2013, **4**, 509-515.

22 A. H. Noor, R. H. Benjamin and A. F. David, *Chem. Commun.*, 2014, **50**, 12389-12391.

23 P. Hohenberg and W. Kohn, *Phys. Rev.*, 1964, **136**, B864-B871.

24 W. Kohn and L. J. Sham, *Phys. Rev.*, 1965, **140**, A1133-A1138.

25 M. D. Segall, P. J. D. Lindan, M. J. Probert, C. J. Pickard, P. J. Hasnip, S. J. Clark and M. C. Payne, *J. Phys.: Condens. Matter*, 2002, **14**, 2717-2744.

26 J. P. Perdew and K. Burke, *Phys. Rev. Lett.*, 1996, **77**, 3865-3868.

27 H. J. Monkhorst and J. D. Pack, *Phys. Rev. B*, 1976, **13**, 5188-5192.

28 D. Vanderbilt, *Phys. Rev. B*, 1990, **41**, 7892-7895.

29 H. Okamoto and T. B. Massalski, *Bull. Alloy Phase Diag.*, 1983, **4**, 30-38.

30 H. M. Lu and Q. Jiang, *Phys. Status Solidi B*, 2004, **241**, 2472-2476.

31 V. A. Lubarda, *Mech. Mater.*, 2003, **35**, 53-68.

32 J. Brillo, I. Egry and I. Ho, *Int. J. Thermophys.*, 2006, **27**, 494-506.

33 http://www.webelements.com/ (Web Elements Periodic Table).

34 C. C. Yang and Y.-W. Mai, *Mater. Sci. Eng. R*, 2014, **79**, 1-40.

35 S. Hassam, M. Gambino, E. Gaune, J. P. Bros and J. Agren, *Metall. Trans. A*, 1988, **19**, 409-416.

36 K. Dick, T. Dhanasekaran, Z. Zhang and D. Meisel, *J. Am. Chem. Soc.*, 2002, **124**, 2312-2317.

37 W. Luo, W. Hu and S. Xiao, *J. Phys. Chem. C*, 2008, **112**, 2359-2369.

Table 1 Related parameters used in the simulations and modeling.

	Au	Ag	$Au_{50}Ag_{50}$
a^S (Å)[31]	4.078	4.086	4.076
E_t^S (eV)	-98678.488	-110991.869	-104844.038
E_a^S (eV)	-910.646	-1025.035	
ε^S (eV)[a]	-0.507	-0.445	-0.490
$\Omega^S(\infty)$ (J·mol^{-1})[b]		-15828.562	
ρ^L (g·cm^{-3})	17.4[32]	9.15[32]	13.3[c]
M (g·mol^{-1})	196.97[33]	107.87[33]	152.42[c]
V_{mol} (cm^3·mol^{-1})[d]	11.320	11.789	11.460
a^L (Å)[e]	4.221	4.279	4.239
E_t^L (eV)	-98684.644	-110989.958	-104845.234
E_a^L (eV)	-910.650	-1025.028	
ε^L (eV)[a]	-0.516	-0.443	-0.492
$\Omega^L(\infty)$ (J·mol^{-1})[b]		-14171.621	
h (nm)[f]	0.2884	0.2889	0.2882
E_b (kJ·mol^{-1})[33]	368	285	
T_b (K)[33]	3129	2435	
S_b (J·mol^{-1}·K^{-1})[g]	117.609	117.043	117.326
$T_m(r = 5\text{nm})$ (K)[h]	1147.643	1060.509	
$H_m(\infty)$ (kJ·mol^{-1})[33]	12.5	11.3	
$H_m(r = 5\text{nm})$ (kJ·mol^{-1})[h]	10.730	9.703	
$\Omega^S(r = 5\text{nm})$ (J·mol^{-1})[h]		-13592.761	
$\Omega^L(r = 5\text{nm})$ (J·mol^{-1})[h]		-12169.865	

[a] ε^S and ε^L are determined by Eq. (3).

[b] $\Omega^S(\infty)$ and $\Omega^L(\infty)$ are determined by Eq. (2a) and (2b), respectively.

[c] For the molar weight M and the liquid density ρ^L of $Au_{50}Ag_{50}$, the average values of those of Au and Ag are used.

[d] $V_{mol} = M/\rho^L$.

[e] The atomic volume can be obtained by $V_a = (V_{mol}\times 10^{24})/N_a$. The volume of unit cells V in FCC crystals is given by $V = 4V_a$, and the lattice parameter in liquid state $a^L = V^{1/3}$.

[f] $h = (2^{1/2}/2)a$ for FCC crystals.

[g] For Au and Ag, $S_b = E_b/T_b$. For $Au_{50}Ag_{50}$, the average value of those of Au and Ag is used.

[h] The values of $T_m(r)$, $H_m(r)$ and $\Omega(r)$ are calculated from Eq. (4).

Captions

Fig. 1 Solid supercell structures of (a) Au, (b) Ag and (c) $Au_{50}Ag_{50}$ after MD simulations with NVT at 300 K. The dark and light balls represent Au and Ag atoms, respectively, and *a* is the lattice parameter of each structure.

Fig. 2 Liquid supercell structures of (a) Au, (b) Ag and (c) $Au_{50}Ag_{50}$ after MD simulations with NVT at 300 K.

Fig. 3 Bulk and nanosized (r = 5 nm) Au-Ag phase diagrams. The solid lines denote predictions from Eq. (1). The symbols ● and ○ are experimental data of the solidus and liquidus curves, respectively.[35] The symbols ∇ are experimental data of $T_m(r)$ for Au nanoparticles (r = 5 nm)[36] and the symbol Δ is a MD simulation result of $T_m(r)$ for Ag nanoparticles (r = 5 nm).[37]

Fig. 1

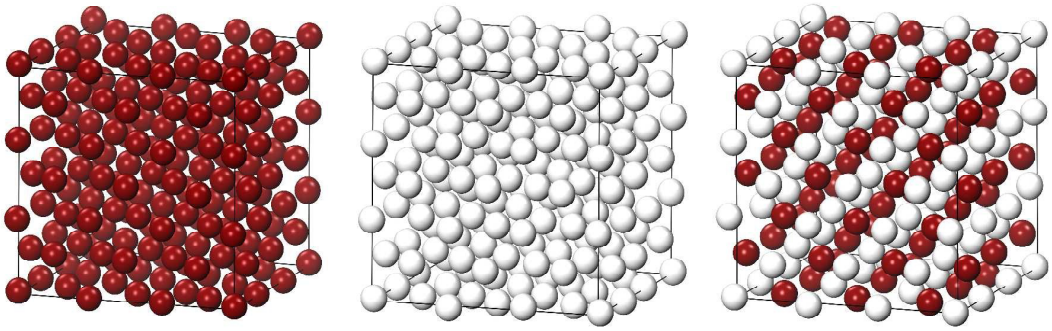

a = 4.078
(a) Au

a = 4.086
(b) Ag

a = 4.076
(c) $Au_{50}Ag_{50}$

Fig. 2

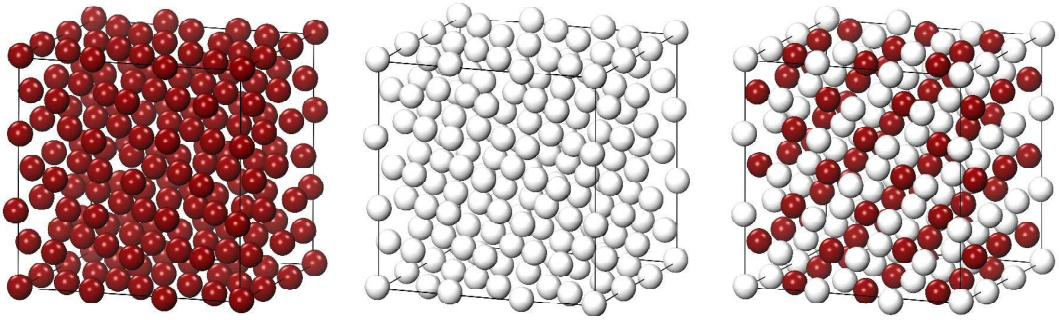

a = 4.221
(a) Au

a = 4.279
(b) Ag

a = 4.239
(c) $Au_{50}Ag_{50}$

Fig. 3

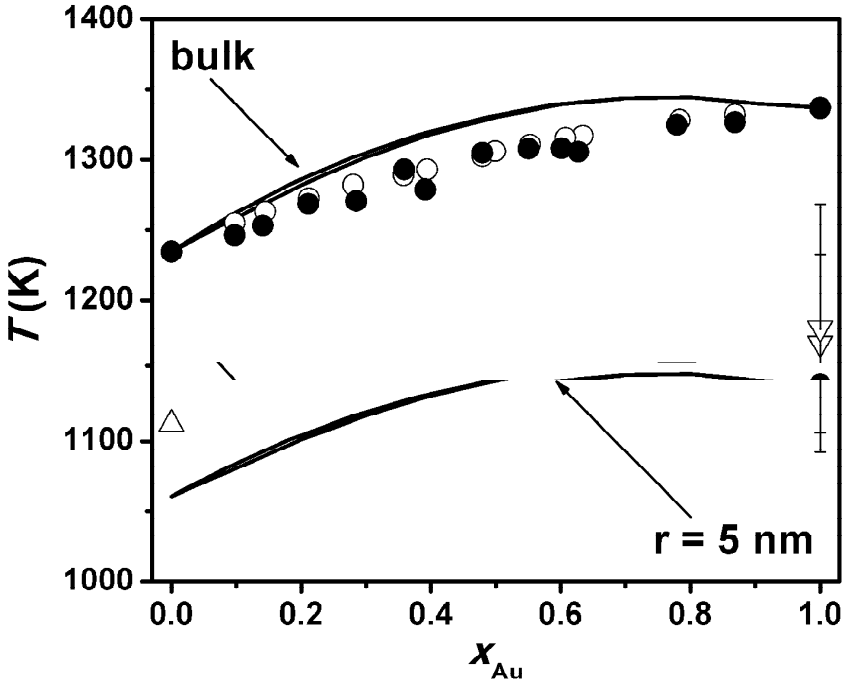

A graphical and textual abstract

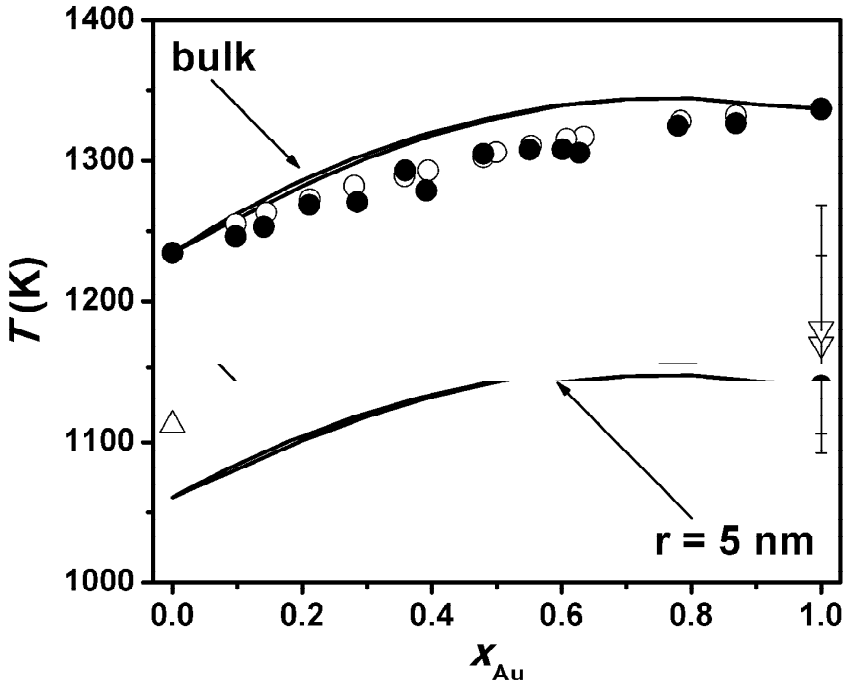

Fig. 3 Bulk and nanosized (r = 5 nm) Au-Ag phase diagrams. The solid lines denote predictions from Eq. (1). The symbols ● and ○ are experimental data of the solidus and liquidus curves, respectively. The symbols ∇ are experimental data of $T_m(r)$ for Au nanoparticles (r = 5 nm) and the symbol Δ is a MD simulation result of $T_m(r)$ for Ag nanoparticles (r = 5 nm).